

# A general relativistic hydrodynamic simulation code for studying advective, sub-Keplerian accretion flow onto black holes

Sudip K Garain<sup>a</sup>

<sup>a</sup>*Department of Physical Sciences and Center of Excellence in Space Sciences India,  
Indian Institute of Science Education and Research  
Kolkata, Mohanpur, Nadia, 741246, WB, India*

---

## Abstract

In this paper, we describe a general relativistic hydrodynamics simulation code which is developed to simulate advective accretion flow onto black holes. We are particularly interested in the accretion simulations of sub-Keplerian matter in the close vicinity of black holes. Due to the presence of centrifugal barrier, a nearly free-falling sub-Keplerian accretion flow slows down close to a black hole and can even pass through shocks before accelerating again to the black hole. We design our simulation code using the high resolution shock capturing scheme so that such shock structures can be captured and analyzed for relevance. In this paper, we describe our implementation and validation of the code against a few known analytical and numerical results of sub-Keplerian matter accretion.

*Keywords:* accretion, accretion disks, black hole physics, hydrodynamics, shock waves, methods: numerical

---

## 1. Introduction

In a black hole X-ray binary (BHXR) system or at the center of a galaxy, usually rotating fluid consisting of mostly plasma is accreted onto a black hole. Strong gravity in the close vicinity of the black hole affects fluid motion in a way that Newtonian potential cannot explain. For example, the effective potential experienced by a rotating particle in the general relativistic

---

*Email address:* sgarain@iiserkol.ac.in (Sudip K Garain)

calculation shows the presence of a finite height potential barrier in contrast to an infinite barrier as in the calculation using Newtonian gravitational field (Misner et al., 1973; Shapiro and Teukolsky, 1983). This barrier is produced by the centrifugal force and the height of this barrier in general relativistic calculation depends on the magnitude of the angular momentum of the particle. Depending on the energy content of the particle, this potential barrier can give rise to a capture orbit or deflect particle away from the black hole or even allow the particle to be accreted by the black hole (Shapiro and Teukolsky, 1983). Though the fluid motion is fundamentally different from a particle motion, such general conclusions derived from particle dynamics also hold for fluid motion. Thus, for the studies of accretion onto black holes, many research groups prefer to solve general relativistic fluid dynamic equations.

Over the past 50 years, several numerical simulation codes for solving the time-dependent general relativistic fluid dynamics equations have been developed (Wilson, 1972; Hawley et al., 1984; Banyuls et al., 1997; Del Zanna and Bucciantini, 2002; Gammie et al., 2003; Font, 2008; Porth et al., 2017, 2019, and references therein). Many of these simulation frameworks assume the total mass of the accretion disk to be negligible compared to the central accretor so that the space-time metric remains unchanged throughout the simulation. Current practice in the accretion disk simulation community is to use an equilibrium thick disk solution threaded by a seed magnetic field as the initial condition (Abramowicz and Fragile, 2013). This seed magnetic field generates some instability inside the disk so that the equilibrium condition is broken and a significant part of matter starts getting accreted onto the black hole.

In contrast to this, one can consider a more realistic set up where the matter comes from, ideally, an infinite distance (e.g, the companion star in the case of BHXR or ISM in the case of black hole at the center of galaxy) to the accreting black hole. Due to limited computational resources, we of course cannot simulate the entire accretion process. So, we simulate the dynamically important inner part of the disk and rely on the analytical solution for the rest of the part. To simulate such a configuration, one considers the matter to enter the simulation domain through the outer boundary located at a finite distance from the black hole. And, inside the simulation domain, the solution of the time-dependent equations self-consistently determines the flow configuration. Thus, one applies an appropriate inflow boundary condition at the outer boundary and supplies the flow parameters there. These inflow

parameters are chosen in such a way that they are consistent with certain analytical solution that extends up to the infinite distance. Several analytical advective accretion solutions are present in literature which connects black horizon with infinite distance (e.g., Bondi accretion solution (Bondi, 1952), slim disk (Abramowicz et al., 1988), hybrid model flows (Chakrabarti, 1989a), ADAF solution (Narayan and Yi, 1994) etc.). Therefore, at the outer boundary of the simulation domain one can use the analytically calculated values of flow parameters using such solutions.

Simulations of purely radial, Bondi type accretion flow does not produce significant variability. Rather, simulations of quasi-spherical, rotating accretion flow show interesting flow features. Accretion disk simulations with Bondi-type density and radial velocity distribution along with an additional, arbitrary latitude-dependent angular momentum component as the inflow boundary condition have been conducted using non-GR (Proga and Begelman, 2003; Janiuk et al., 2008; Li et al., 2013) as well as GR codes (Suková et al., 2017; Ressler et al., 2021; Lalakos et al., 2022; Kaaz et al., 2023; Cho et al., 2023; Olivares et al., 2023; Dihingia and Mizuno, 2024). We are rather interested in solutions of rotating flows which self-consistently takes the matter rotation into account. Steady state solutions, extending from horizon to infinity, of the rotating fluids with sub-Keplerian angular momentum (at a large distance from a black hole) are present in literature (Fukue, 1987; Chakrabarti, 1989b). The solution shows that the centrifugal barrier can slow down the nearly free fall motion of the flow close to the black hole. This barrier can even force the fluid to pass through shocks before being accreted. These solutions are advective and show significantly high value of radial velocity except near the shock location where the flow is nearly halted. When the angular momentum is set to zero, the solution becomes identical to the standard Bondi accretion solution.

Numerical simulations of this flow in the close vicinity of the black holes have resulted in a dynamical flow configuration which can explain several observational features (Molteni et al., 1994; Ryu et al., 1997; Chakrabarti et al., 2004; Garain et al., 2014; Das et al., 2014; Lee et al., 2016; Patra et al., 2019; Debnath et al., 2024). Many of these simulation works are done using pseudo-Newtonian potential proposed in Paczyński and Wiita (1980). This potential reproduces the effective potential around a non-rotating black hole satisfactorily well. However, being non-general relativistic, it has several drawbacks compared to the Schwarzschild spacetime. For example, computations show that the fluid bulk velocity can become super-luminal close to the

horizon. Additionally, the effects of space-time dragging due to black hole rotation cannot be investigated. For these reasons, it is beneficial to study such accretion flow using a general relativistic fluid solver in the Kerr background. A few simulation results for this kind of flow with above-mentioned set-up are reported in Kim et al. (2017a, 2019). However, further extensions are not reported. In this paper, we describe the development of a general relativistic hydrodynamics simulation code, designed specifically to implement the above set-up and study such advective flow. We provide results of several validating test problems where we compare the numerical solutions obtained using this simulation code with the analytical solutions for the above mentioned advective flow.

Our paper is organized as follows: In Section 2, we provide a very brief overview of the general relativistic analytical solution of the sub-Keplerian accretion flow. We shall use these solutions as our benchmark test problems. In Section 3, we introduce the time-dependent general relativistic hydrodynamics (GRHD) equations and our numerical solution methodology. In Section 4, we present the results. Finally, in Section 5, we provide a summary and our concluding remarks.

In our following calculations, we use  $r_g = GM_{bh}/c^2$  as unit of distance,  $r_g/c$  as unit of time and  $r_gc$  as unit of specific (i.e., per unit mass) angular momentum. Specific energy is measured in the unit of  $c^2$ . Here,  $G$  is the gravitational constant,  $M_{bh}$  is the mass of the black hole and  $c$  is the speed of light in vacuum.

## 2. Theory of Sub-Keplerian advective flow

General relativistic, steady state sub-Keplerian advective flow solution is discussed in great details in many references (Chakrabarti, 1990, 1996a,c,b). Here, we provide a very brief discussion for the sake of completeness. Analytical solution aims to find the radial variation of solution variables under various flow models such as wedge flow, constant height flow and vertical equilibrium. For analytical studies, we use the following form of Kerr metric (valid only near the equatorial plane) expressed in cylindrical coordinates:

$$\begin{aligned}
 ds^2 &= g_{\mu\nu} dx^\mu dx^\nu \\
 &= -\frac{r^2 \Delta}{\delta} dt^2 + \frac{\delta}{r^2} (d\phi - \omega dt)^2 + \frac{r^2}{\Delta} dr^2 + dz^2
 \end{aligned}
 \tag{1}$$

(Novikov and Thorne, 1973). Here,

$$\delta = r^4 + r^2 a^2 + 2ra^2, \quad \Delta = r^2 - 2r + a^2, \quad \omega = 2ar/\delta,$$

$a$  being the spin parameter of the black hole.

Steady state solution of non-dissipative sub-Keplerian advective flow is derived using the conservation equations of mass accretion rate  $\dot{m}$  and specific energy  $\epsilon$ :

$$\dot{m} = \rho u^r A \tag{2}$$

$$\epsilon = hu_t = \frac{1}{1 - na_s^2} u_t. \tag{3}$$

Here,  $\rho$  is the rest-mass density,  $u^r$  is  $r$  component of the four-velocity  $u^\mu$ ,  $A$  is a geometric quantity representing the surface area through which mass flux is considered. For different flow models,  $A$  may have different expressions.  $h = 1/(1 - na_s^2)$  represents the enthalpy with  $a_s$  being the sound speed.  $u_t$  is the  $t$  component of the four velocity  $u_\mu$  and is obtained using the normalization  $u^\mu u_\mu = -1$  as follows:

$$u_t = \left[ \frac{\Delta}{(1 - V^2)(1 - \Omega l)(g_{\phi\phi} + lg_{t\phi})} \right]^{1/2}. \tag{4}$$

Here,  $\Omega$  is the angular velocity of the rotating fluid

$$\Omega = \frac{u^\phi}{u^t} = -\frac{g_{t\phi} + lg_{tt}}{g_{\phi\phi} + lg_{t\phi}}, \tag{5}$$

and  $l = -u_\phi/u_t$  is the specific angular momentum (angular momentum per unit mass) and it is a conserved quantity. Also, the radial velocity  $\mathcal{V}$  in the rotating frame is

$$\mathcal{V} = \frac{v}{(1 - \Omega l)^{1/2}}, \tag{6}$$

where

$$v = \left( -\frac{u_r u^r}{u_t u^t} \right)^{1/2}. \tag{7}$$

Next, one takes derivative of  $\dot{m}$  and  $\epsilon$  w.r.t.  $r$  and eliminates  $da_s/dr$  from both the equations and finally, obtains an equation for  $d\mathcal{V}/dr$ . Imposition of transonic condition in this equation enables us to find the critical (transonic)

points. This imposition implies that such a transonic solution depends only on two conserved parameters out of three, namely,  $\dot{m}$ ,  $\epsilon$  and  $l$  (Chakrabarti, 1990).

The equation of  $d\mathcal{V}/dr$  is numerically solved to find  $\mathcal{V}(r)$ . For certain combinations of flow parameters  $\epsilon$  and  $l$ , the solutions show presence of two X-type critical points. For accretion or wind solution, a solution branch passing through the outer critical point and a solution branch passing through the inner critical point may be connected via a shock jump. The shock location is found by applying Rankine-Hugoniot condition. Fig. 1 shows radial variation of Mach number  $\mathcal{V}/a_s$  for the accretion and the wind solutions for a Kerr black hole with spin parameter  $a = 0.99$ . Fig. 1(a) shows the example of the accretion solution. This is done for  $\epsilon = 1.01$  and  $l = 2.073$ . Red solid line shows the solution branches passing through the outer critical point located at  $r = 71.84$  and the blue solid line shows the same passing through the inner critical point located at  $r = 1.38$ . The shock location at  $r = 3.6$  is shown by the dashed line. The arrows indicate the solution branches followed by the accreting matter. Similarly, Fig. 1(b) shows an example of the wind solution. This is done for  $\epsilon = 1.03$  and  $l = 2.1$ . Line styles are same as in Fig. 1(a). The outer critical point, the inner critical point and the shock locations are 21.26, 1.32 and 1.87 respectively. We are going to use these analytical solutions for benchmarking our code.

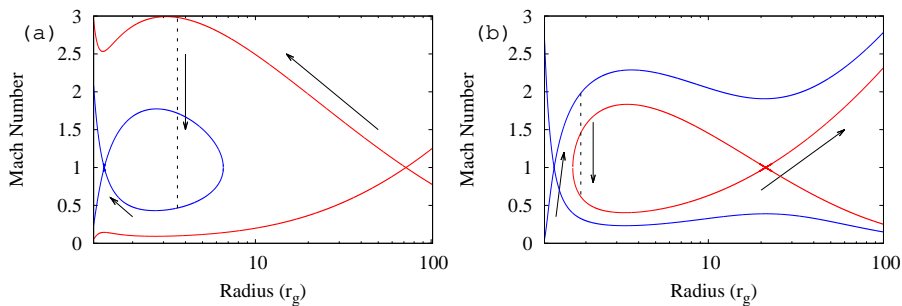


Figure 1: a) shows the radial variation of Mach number  $\mathcal{V}/a_s$  for an accretion solution, whereas, b) shows the same for a wind solution. In both the Figures, the arrows indicate the solution branches followed by the flow. See text for details.

### 3. GRHD: Basic equations and solution procedure

GRHD equations are derived from the following conservation laws:

$$\nabla_{\mu}(\rho u^{\mu}) = 0 \quad (8)$$

$$\nabla_{\mu}T^{\mu\nu} = 0 \quad (9)$$

Here,  $\nabla_{\mu}$  represents the covariant derivative,  $u^{\mu}$  is the four-velocity and  $T^{\mu\nu}$  is the stress-energy tensor.  $T^{\mu\nu} = \rho h u^{\mu} u^{\nu} + P g^{\mu\nu}$  for ideal fluid with  $h$  as the specific enthalpy given by  $h = 1 + \frac{\Gamma}{\Gamma-1} \frac{P}{\rho}$ ,  $\Gamma = 4/3$  being the adiabatic index and  $P$  being the pressure. The first equation represents the conservation of baryon number and the second equation is the conservation of energy-momentum tensor.

Following {3+1} formalism (Banyuls et al., 1997; Font, 2008), we write the space-time metric  $g_{\mu\nu}$  in terms of lapse ( $\alpha$ ), shift vector ( $\beta^i$ ) and the spatial metric ( $\gamma_{ij}$ ). After some algebraic manipulations, this set of equations can be written as a set of five partial differential equations (PDEs):

$$\begin{aligned} \frac{1}{\sqrt{-g}} \left[ \frac{\partial \sqrt{\gamma} D}{\partial t} + \frac{\partial}{\partial x^i} \left( \sqrt{-g} D \left( v^i - \frac{\beta^i}{\alpha} \right) \right) \right] &= 0 \quad (10) \\ \frac{1}{\sqrt{-g}} \left[ \frac{\partial \sqrt{\gamma} S_j}{\partial t} + \frac{\partial}{\partial x^i} \left( \sqrt{-g} \left( S_j \left( v^i - \frac{\beta^i}{\alpha} \right) + P \delta_j^i \right) \right) \right] &= T^{\mu\nu} \left( \frac{\partial g_{\nu j}}{\partial x^{\mu}} - \Gamma_{\nu\mu}^{\lambda} g_{\lambda j} \right) \quad (11) \\ \frac{1}{\sqrt{-g}} \left[ \frac{\partial \sqrt{\gamma} \tau}{\partial t} + \frac{\partial}{\partial x^i} \left( \sqrt{-g} \left( \tau \left( v^i - \frac{\beta^i}{\alpha} \right) + P v^i \right) \right) \right] &= \alpha \left( T^{\mu 0} \frac{\partial \ln \alpha}{\partial x^{\mu}} - T^{\mu\nu} \Gamma_{\mu\nu}^{\rho} \right) \quad (12) \end{aligned}$$

Here,  $\sqrt{-g} \equiv \det(g_{\mu\nu})$  and  $\sqrt{\gamma} \equiv \det(\gamma_{ij})$ , and these are connected by  $\sqrt{-g} = \alpha \sqrt{\gamma}$ . We denote the set of five-component vector  $U = (D, S_j, \tau)$  as vector of conserved variables and can be expressed in terms of vector of primitive variables  $V = (\rho, v^i, P)$  as follows:

$$D = \rho W, \quad S_j = \rho h W^2 v_j, \quad \tau = \rho h W^2 - P - D.$$

Here,  $W$  is the Lorentz factor given by  $W = 1/\sqrt{1 - v^i v_i} = \alpha u^t$ .  $v^i$  are the components of three-velocity given as  $v^i = \frac{u^i}{\alpha u^t} + \frac{\beta^i}{\alpha}$  and the co-variant counterpart can be calculated as  $v_j = \gamma_{ij} v^i$ .

The above set of PDEs is further written in integral form and subsequently discretised on a given mesh (Banyuls et al., 1997; Font, 2008). The resulting discretised equations on a spherical mesh constructed using Boyer–Lindquist coordinates  $(t, r, \theta, \phi)$  (Boyer and Lindquist, 1967) are solved using finite

volume method. For our present calculations, we use the following form of the Kerr space-time metric:

$$g_{\mu\nu} = \begin{bmatrix} -(1 - \frac{2r}{\sigma}) & 0 & 0 & -\frac{2ar \sin^2 \theta}{\sigma} \\ 0 & \frac{\sigma}{\Sigma} & 0 & 0 \\ 0 & 0 & \sigma & 0 \\ -\frac{2ar \sin^2 \theta}{\sigma} & 0 & 0 & (r^2 + a^2 + \frac{2ra^2 \sin^2 \theta}{\sigma}) \sin^2 \theta \end{bmatrix},$$

where,  $\sigma = r^2 + a^2 \cos^2 \theta$  and  $\Sigma = r^2 - 2r + a^2$ . With these notations, the lapse  $\alpha$  and shift  $\beta^i$  functions are as follows:

$$\alpha = \sqrt{\frac{\sigma \Sigma}{(r^2 + a^2)\sigma + 2ra^2 \sin^2 \theta}},$$

$$\beta^r = \beta^\theta = 0, \quad \beta^\phi = -\frac{2ar}{(r^2 + a^2)\sigma + 2ra^2 \sin^2 \theta}.$$

Also, the determinant of the metric is

$$\sqrt{-g} = \sigma \sin \theta / \alpha$$

This hydrodynamics simulation code is an extension of our non-GR code used in a previous work (Garain and Kim, 2023). We improve several sub-routines suitably to incorporate general relativistic effects. For spatial reconstruction, we have used second order accurate van Leer slope limiter following (Mignone, 2014). We perform reconstruction on vector  $(\rho, Wv^i, P)$ , instead of primitive variable vector  $V$ , since the reconstruction on  $Wv^i$  ensures sub-luminal reconstructed profile of  $v^i$  inside a zone (Balsara and Kim, 2016). We have provisions for HLL and LLF Riemann solvers for calculating the interfacial fluxes. For all the presented results, we use HLL Riemann solver. Second-order accurate strong stability preserving Runge-Kutta(RK) time integration is used for time advancement. One of the non-trivial step in GRHD is the conserved-to-primitive conversion as it requires a non-linear equation solution employing a root solver (e.g., Newton-Raphson). We have implemented two methods following Mignone and Bodo (2005) and Del Zanna and Bucciantini (2002). For our calculations, we prefer the method of Del Zanna and Bucciantini (2002). It may happen that the root solver does not converge for a few zones after the time-update step and for such zones, we use the previous time-step solution as it is already saved in a RK type time-update. The

timestep  $dt$  is calculated following standard Courant-Friedrichs-Lewy (CFL) condition (LeVeque, 2002; Toro, 2009)

$$dt = C_{\text{CFL}} \frac{1}{\frac{\lambda^r}{dr} + \frac{\lambda^\theta}{rd\theta} + \frac{\lambda^\phi}{r \sin\theta d\phi}},$$

where,  $\lambda^i$  is maximum characteristic speed in  $i^{\text{th}}$  direction and  $C_{\text{CFL}}$  is the CFL number. For all the runs, we use  $C_{\text{CFL}} = 0.9$ . For one- or two-dimensional simulations, contribution from the corresponding inactive dimension(s) is switched off.

## 4. Results

In this section, we present results of a few standard test problems validating our implementation. Later in this section, we present results of multi-dimensional simulation for sub-Keplerian advective accretion disk.

### 4.1. Accuracy analysis using two-dimensional equilibrium torus:

Equilibrium torus is a hydrostatic equilibrium solution of the above mentioned GRHD equations. The solution results in a geometrically thick disk around a gravitating source and the matter is held at its position because of the balance between the inward gravitational pull and the combined effect of outward centrifugal and pressure gradient forces. General procedure for the construction of such disks is given in many papers, e.g., Abramowicz et al. (1978); Chakrabarti (1985); Font and Daigne (2002) etc. In this work, we consider a constant angular momentum disk and calculate the density, pressure and velocity distributions following the analytical calculations given in the above references. Next, we initialize our computational domain with these distributions and run our simulation for some time. Since this is a time-steady solution, we expect the values of these variables to remain same at all positions. However, due to inherent errors of the numerical solution scheme, the numerical solution is expected to develop error.

We conduct several two dimensional  $(r, \theta)$  simulations of such thick disk around black holes with different spin parameters. Here, we show results for two cases, (1) with spin parameter  $a = 0$  and (2) with  $a = 0.99$ . In our simulations, we maintain the initial state of the solutions at the ghost zones of both the radial boundaries throughout the simulations. Such fixed boundary

conditions have been used previously for global accuracy convergence demonstrations (Mignone, 2014; Fambri et al., 2018; Balsara et al., 2018, 2020). On the  $\theta$  boundaries, we use reflection boundary condition.

For case (1), we choose the constant specific angular momentum to be  $l = 3.9$ . This disk has a cusp at around 4.3 and the disk center is located around 9.3. We use inner edge of the disk at 4.5 while calculating the fluid variables so that the disk does not fill up the Roche lobe. For accuracy analysis, the simulations are run on varying grid sizes ranging from  $[32 \times 45]$  to  $[512 \times 720]$  on a  $r - \theta$  domain  $[7:15] \times [\pi/4:3\pi/4]$ . The disk center is located inside our computational domain. Fig. 2(a) shows the density distribution for this case at the final time  $t = 100$ . This result is drawn for the simulation with grid size  $[128 \times 180]$ . Fig. 3(a) shows the result of the accuracy analysis in the density variable. Purple line shows the convergence result for  $L_1$  error while green line shows the same for  $L_{inf}$  error. The reference slope is also provided for comparison.

For case (2), we choose  $l = 2.19$ . This disk has a cusp at around 1.22 and the disk center is located around 1.94. We use inner edge of the disk at 1.22 for this case. The simulations are run in the  $r, \theta$  domain  $[1.45:4.45] \times [\pi/4:3\pi/4]$  on grid cells  $[30 \times 30]$  to  $[480 \times 480]$ . Fig. 2(b) shows the density distribution for this case at the final time  $t = 100$ . This result is drawn for the simulation with grid size  $[120 \times 120]$ . Fig. 3(b) shows the result of the accuracy analysis in the density variable. Purple line shows the convergence result for  $L_1$  error while green line shows the same for  $L_{inf}$  error. The reference slope is also provided for comparison.

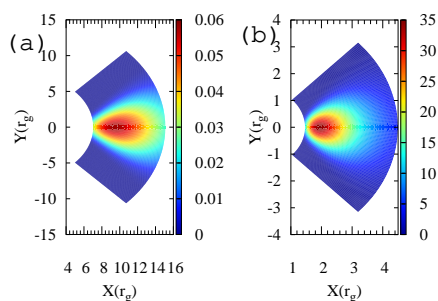


Figure 2: (a) shows the density distribution inside the thick disk at the final time  $t = 100$  for the case with spin  $a = 0$ . The disk center is located around 9.3. (b) shows the same at  $t = 100$  for the case with spin  $a = 0.99$ . The disk center is located around 1.94.

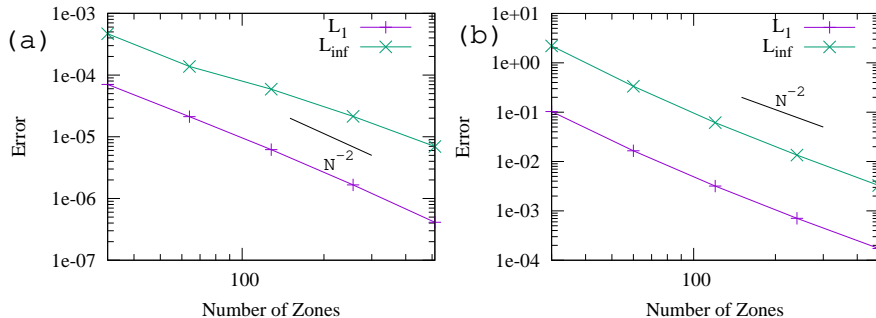


Figure 3: Accuracy demonstration for torus problem: (a) shows the  $L_1$  and  $L_{inf}$  error convergence results for the case with spin  $a = 0$ . (b) shows the same for the case with spin  $a = 0.99$ .

#### 4.2. Shock in one-dimensional advective flow:

Here we demonstrate our code’s capability to reproduce the steady state advective flow solutions having a shock. First, we compare the analytical solution of a constant, low-angular momentum (sub-Keplerian) accretion flow onto a black hole with the numerically simulated one. Next, we perform similar comparison for a wind solution.

Sub-Keplerian accretion solution connects infinity to the black hole horizon. The subsonic matter at far away (infinite) distance accelerates to supersonic speed at a finite distance (sonic point) from black hole before it reaches the black hole horizon. As discussed in Section 2, if the flow specific energy ( $\epsilon$ ) and specific angular momentum ( $l$ ) fall within certain parameter space, the flow may pass through a shock after crossing the sonic point. In such case, the matter accelerates soon to become supersonic again at certain radius (inner sonic point) before reaching the horizon.

For our comparison, we choose flow parameters such that the solution contains a shock. Theoretically, solution branches passing through the outer and the inner sonic points have different entropies (Chakrabarti, 1989a): solution through the inner sonic point has higher entropy than that through the outer one. Thus, thermodynamically, as the matter approaches the black hole, it prefers to follow the solution through the inner sonic point. However, note from Fig. 1(a) that the solution through the inner sonic point (blue solid line) does not extend up to infinite distance. Thus, the matter coming from infinite distance initially follows the solution passing through the outer sonic point. However, when the matter arrives sufficiently close to the black hole so

that solution through inner sonic point is available, it makes a transition to this solution. The required excess entropy is produced at the shock and that allows matter to jump from the branch passing through the outer sonic point to the branch passing through the inner sonic point. In a realistic three-dimensional flow, the matter bouncing off the centrifugal barrier collides with the incoming matter and makes the flow turbulent. This generates the required excess entropy (Chakrabarti and Molteni, 1993).

Shocks in an accretion flow can form at a few hundreds to only a few  $r_g$  distance depending on  $(\epsilon, l)$  pair. Capturing a shock very close a black hole is one of the stringent tests. In Fig. 4(a), we show that our simulation code can capture a shock at  $r = 3.5$ . Radial variation of Mach number is shown in this plot. We see that the shock is resolved within one grid point. This solution corresponds to  $\epsilon = 1.01$  and  $l = 2.073$ . Solid line shows the analytical solution (solution marked by arrows in Fig. 1(a)) and the crosses are the numerically simulated solution. This simulation is carried out using 300 logarithmically binned grid cells inside the domain [1.2:80]. Black hole spin is assumed to be  $a = 0.99$ . We use out-flow boundary condition at the inner edge and inflow boundary condition at the outer edge. We use two ghost cells for our computation. The centroids of these cells are located at 80.566 and 81.702. As the inflow boundary, we maintain  $V = (1, 7.303E - 2, 0, 3.153E - 4, 4.9089E - 3)$  at the first cell and  $V = (0.985, 7.213E - 2, 0, 3.067E - 4, 4.808E - 3)$  at the second cell throughout the simulation. Initially, the computation domain is filled with static matter with  $\rho = \rho_{\text{floor}} = 10^{-8}$  and  $P = P_{\text{floor}} = a_s^2 * \rho_{\text{floor}} / \gamma$  where  $a_s = 0.0802$  is the sound speed at the outer radial boundary.  $\gamma = 4/3$  is assumed for this run. Thus, as the simulation is started, matter rushes towards the black hole and within a few hundred  $r_g/c$  time, simulation domain is filled up with matter that corresponds to the analytical solution passing through the outer sonic point. Since one-dimensional flow doesn't develop turbulence, this solution does not pass through the shock and the inner sonic point. Thus, to produce shock in a one-dimensional flow, we need to momentarily apply some perturbation such that the flow acquires sufficient additional entropy to pass through the inner sonic point (Chakrabarti and Molteni, 1993). Once the flow passes through the inner sonic point, it automatically develops a shock which ultimately settles down close to the theoretically predicted location. In our simulation, this perturbation is applied at the inflow boundary: we momentarily (for a duration of 30  $r_g/c$ ) increase the pressure by a factor of 9 in the two outer radial boundary ghost cells at around time  $t = 4000$ . This

perturbation is advected with the flow and makes it pass through the inner sonic point and a stable solution passing through the shock is developed by time  $t = 7000$ . We run the simulation till a stopping time of  $t = 50000$  just to ensure that it is actually a steady state. Analytical calculation provides the location of outer sonic point, shock and inner sonic points at 71.84, 3.6 and 1.38, respectively. Our numerical calculation captures the outer and inner sonic points exactly at these locations as can be seen in Fig. 4(a). The numerical calculation finds the shock at 3.5.

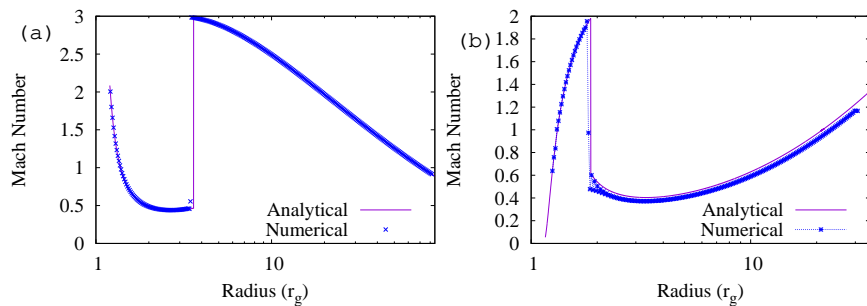


Figure 4: (a) shows the shock in accretion flow solution, whereas, (b) shows the same in wind solution. See text for details.

Just like the accretion flow solution can pass through a shock, a wind solution can also pass through a shock close to the black hole if the  $\epsilon$  and  $l$  values for the solution are chosen within a certain range. Fig. 4(b) shows the simulation of such a wind solution. Radial variation of Mach number is shown in this plot. This solution corresponds to  $\epsilon = 1.03$  and  $l = 2.1$ . Solid line shows the analytical solution (solution marked by arrows in Fig. 1(b)) and the crosses are the numerically simulated solution. This simulation is carried out using 200 logarithmically binned grid cells inside the domain  $[1.28:30]$ . Black hole spin is taken to be  $a = 0.99$  for this case. For simulating wind solution, matter is launched from very close to the black hole and it flies off to infinite distant. Thus, we use inflow boundary condition at the inner radial boundary and outflow boundary condition at the outer radial boundary. We use two ghost cells for our computation. The centroids of the two inner ghost cells are located at around  $r = 1.25$  and  $r = 1.27$ . As the inflow boundary, we maintain  $V = (1.317, 0.0305, 0, 0.2725, 0.187)$  in the first cell and  $V = (1, 0.0384, 0, 0.2756, 0.1297)$  in the second cell throughout the simulation. As the initial condition, we fill up part of the simulation

domain  $[1.28:r_b]$  with analytical solutions passing through the inner sonic point and the rest  $[r_b:30]$  with the analytical solution passing through the outer sonic point. Thus, the initial state has a shock discontinuity at  $r_b$ . For result shown in Fig. 4(b), we use  $r_b = 3$ . With this initial state, we start the simulation and within time around  $t = 2000$ , the shock discontinuity settles down at a radius  $r = 1.87$  which is very close to the theoretically predicted shock location  $= 1.82$ . Note that for this case, the shock is inside the ergosphere. For our code, we find the solution immediately after the shock is oscillatory. Possibly, this can be avoided by using higher order spatially accurate reconstruction. We run the simulation till a stopping time of  $t = 10000$  just to ensure that it is actually a steady state. We have simulated different cases with different values of  $r_b$  and ensure that this steady state solution is independent of  $r_b$  value.

#### 4.3. Two-dimensional Bondi accretion flow:

This test problem is adapted from Kim et al. (2019). In this problem, we show the effect of spacetime dragging close to a rotating black hole. Because of this dragging, a spherically symmetric accretion configuration onto a rotating black hole develops axisymmetry close to the black hole (see also Aguayo-Ortiz et al. (2021)).

This simulation is performed on a  $r-\theta$  computation domain  $[1.35:200] \times [0:\pi]$  using  $300 \times 180$  grid cells. In the  $r$  direction, we use logarithmic binning and in the  $\theta$  direction, grids are equispaced. Spin parameter of the black hole is assumed to be  $a = 0.99$ . The boundary conditions are same as in Kim et al. (2019). Matter enters simulation domain with  $\mathcal{V} = 0.0229$  and  $a_s = 0.0805$  at  $r_{\text{out}} = 200$ . This corresponds to  $\epsilon = 1.015$  and  $l = 0$ . At the inner radial boundary, we use zero gradient outflow boundary condition. At the  $\theta$  boundaries, we use reflecting boundary conditions. The simulation is run till a stopping time of 20000. By this time, a steady state solution has developed.

In this test problem, matter is injected into the simulation domain spherically symmetrically. In the absence of black hole rotation, such accretion solution remains spherically symmetric by the time it crosses the horizon. However, a rotating black hole drags the spacetime around it and hence breaks the spherical symmetry and makes the accretion solution axisymmetric. Such axisymmetry can be visualized in the fluid variables such as density distribution. To quantify this, we plot the distribution of  $(\rho(r, \theta) - \rho_{\text{eq}}(r, \pi/2)) / \rho_{\text{eq}}(r, \pi/2)$ , where,  $\rho_{\text{eq}}(r, \pi/2)$  is the density at  $(r, \theta = \pi/2)$ , in the inner part of the simulation domain. Colors in Fig. 5(a) show this quantity. We can clearly see

that, at a given radius  $r$ ,  $\rho$  towards the polar region is less than  $\rho$  at the equator. The maximum difference between the density values is nearly 14% for this simulation. We also trace the density iso-contours on the  $r - \theta$  plane in Fig. 5(b). On the x-axis, we plot polar angle  $\theta$  and on the y-axis, we plot the radial coordinate  $r$  normalized by  $r$  on the axis for a given density value. Contours are drawn for density values 50, 100, 150, 200 and 250 (from bottom to top). This plot shows that same density value appears at larger  $r$  on the equator than on the poles. For example, highest density value 250 appears at 7.8% higher  $r$  on the equator than on the poles. This Fig. can be compared with Fig. 2(b) of Kim et al. (2019) who obtained a value slightly higher than 7% (less than our value of 7.8%). This is caused by our choice of higher black hole spin  $a = 0.99$  compared to their  $a = 0.95$ . Frame dragging induces axisymmetric rotation  $\Omega(r, \theta) = u^\phi/u^t$  although specific angular momentum  $l = -u_\phi/u_t$  is zero for this flow. Fig. 5(c) shows the distribution of  $(\Omega(r, \theta) - \Omega_{\text{eq}}(r, \pi/2))/\Omega_{\text{eq}}(r, \pi/2)$ , as in Fig. 5(a). We see that  $\Omega$  is lesser towards the pole.

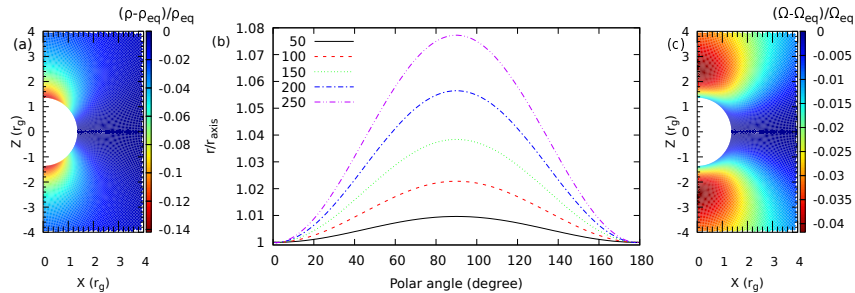


Figure 5: (a) shows the distribution of relative density w.r.t equatorial density at final time  $t = 20000$ , (b) shows the radial coordinate  $r$  normalized by  $r$  on axis for a given density value as a function of polar angle, (c) shows the distribution of relative  $\Omega$  w.r.t equatorial  $\Omega$ . See text for details.

#### 4.4. Two-dimensional sub-Keplerian accretion flow:

This is the multi-dimensional extension of the one-dimensional advective flow discussed in Section 2. In multi-dimensional simulations, one gets an opportunity to study the vertical structure of the geometrically thick sub-Keplerian advective flow. The simulation procedure is nearly same as the above mentioned two-dimensional Bondi accretion flow. Only difference is at the implementation of the outer radial boundary condition. Instead of

spherically symmetric inflow at the outer boundary, we now inject matter axisymmetrically. Additionally, to allow outflow from the accretion disk through the outer boundary, we restrict matter injection within  $-10^\circ \leq (\theta - 90^\circ) \leq 10^\circ$  and apply zero gradient outflow boundary condition otherwise.

This simulation has been performed on a  $r - \theta$  domain  $[1.35:100] \times [0:\pi]$  using  $200 \times 180$  grid cells. In the radial direction, we use logarithmic binning and in the  $\theta$  direction, we use uniform mesh. Black hole spin is assumed to be  $a = 0.99$ . Matter enters simulation domain with  $\mathcal{V} = 0.0666$  and  $a_s = 0.0647$  at  $r_{\text{out}} = 100$ . This corresponds to  $\epsilon = 1.005$  and  $l = 2.05$ . This simulation has been run till a stopping time of 20000. Solution has reached a time-steady state by this time.

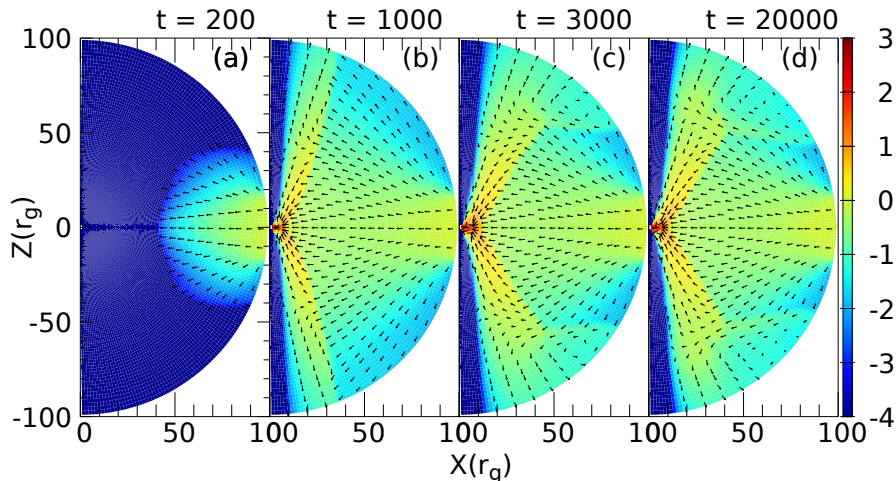


Figure 6: Time-evolution of density distribution on a logarithmic scale for sub-Keplerian accretion disk simulation. Arrows show the velocity field.

Fig. 6 shows the sequence of snapshots at progressing time. Colors show  $\log_{10}\rho$  and arrows show the direction of velocity vectors  $(v^r, v^\theta)$ . Length of an arrow is proportional to the logarithm of its magnitude. Timestep is marked on top of each Figure. Fig. 6(a) shows a transient state when the matter rushes towards the black hole sitting at the origin through nearly vacuum. Fig. 6(b), again a transient state, shows the building of centrifugal force supported boundary layer. The boundary layer can be identified by tracing the density jump as we move vertically away from the equator. Initially, this boundary layer expands in the radial direction and finally settles down. By

the time the solution reaches the state of Fig. 6(c), solutions becomes steady and this state continues till the end of simulation in Fig. 6(d). The evolution is very much consistent with the earlier simulations with non-rotating black holes (e.g., Kim et al. (2017b)) as well as rotating black holes (e.g., Kim et al. (2019)) with lower spin ( $a = 0.95$ ) than the present one ( $a = 0.99$ ).

Fig. 7 shows the radial variation of the vertically averaged Mach number at the final time. Simple averaging of the Mach number values has been done over 4 grid cells above and below the equator. Clearly, the accretion flow develops a shock (supersonic to subsonic transition) around  $r = 10$ . Additionally, we find another shock between  $r = 2 - 3$  for this case. Presence of such an inner shock in multi-dimensional simulations has been reported earlier for non-rotating black holes (Giri et al., 2010; Lee et al., 2011) where simulations are carried out using pseudo-Newtonian Paczyński and Wiita (1980) potential. However, for a rotating black hole and using a truly GRHD simulation, we find such an inner shock extremely close to the horizon. Though, as reported in Cruz-Osorio et al. (2012), placement of inner boundary outside of event horizon may affect the flow dynamics and the inner shock formation. More elaborated analysis of such inner shocks and their observational consequences will be discussed in future works.

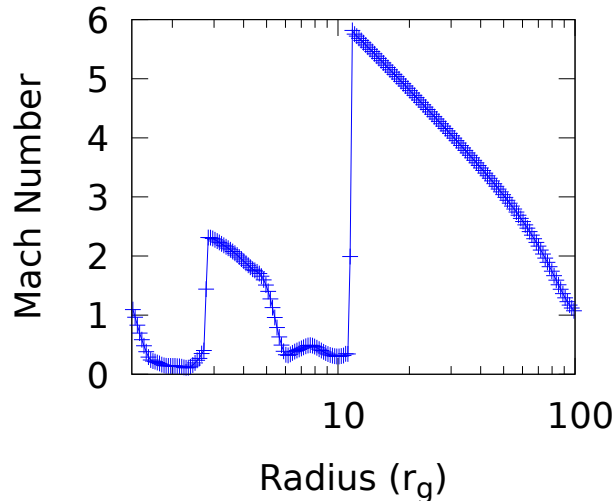


Figure 7: Radial variation of the Mach number along the equator at the end of the sub-Keplerian accretion flow simulation.

## 5. Summary and Conclusions

In this paper, we present a general relativistic hydrodynamics (GRHD) solver. Our aim is to use the said solver for simulating an advective accretion disk configuration that mimics mass inflow from far out rather than starting from an equilibrium torus. In this solver, we solve the GRHD equations using finite volume method on a discretised mesh inside a given computational domain. This method incorporates high resolution shock capturing schemes.

We have demonstrated that our presently developed GRHD code works for Kerr spacetime, is globally second order accurate and performs robustly in multi-dimensions. For demonstrating global accuracy, we compute the numerical errors using a hydrostatic equilibrium, geometrically thick disk configuration and find the errors converge with second order accuracy. We also demonstrate that our scheme can correctly capture the analytically predicted accretion and wind shock solutions around a rotating black hole. In both the cases, shocks are resolved within one or two grid points. Specifically, we demonstrate that our solver can capture the shocks extremely close to the black hole (even inside the ergosphere). Next, we demonstrate the effects of spacetime dragging in the close vicinity of an extremely rotating black hole (with spin parameter  $a = 0.99$ ). We show that a spherically symmetric accretion becomes axi-symmetric as the matter approaches the black hole. Finally, we show an example where we simulate a geometrically thick sub-Keplerian accretion disk. We allow rotating matter to enter the simulation domain through a part of the outer radial boundary (close to the equatorial region) and also allow outflow through rest of the outer radial boundary (close to the poles). The accreting matter rushes to the black hole through nearly vacuum and self-consistently forms a shock due to centrifugal barrier. The post-shock matter forms a thick disk. The present solution shows formation of two shocks close to the black hole. In subsequent works, we shall explore these thick disk solutions in great details and investigate their radiative properties.

## 6. Acknowledgments

We acknowledge the usage of Kepler cluster of DPS, IISER Kolkata and Pegasus cluster of IUCAA, Pune for running a few simulations. Author also acknowledges the help of Mr. Pranayjit Dey during the initial days of the code development.

## References

- Abramowicz, M., Jaroszynski, M., Sikora, M., 1978. Relativistic, accreting disks. *A&A* 63, 221–224.
- Abramowicz, M.A., Czerny, B., Lasota, J.P., Szuszkiewicz, E., 1988. Slim Accretion Disks. *ApJ* 332, 646. doi:10.1086/166683.
- Abramowicz, M.A., Fragile, P.C., 2013. Foundations of Black Hole Accretion Disk Theory. *Living Reviews in Relativity* 16, 1. doi:10.12942/lrr-2013-1, arXiv:1104.5499.
- Aguayo-Ortiz, A., Tejeda, E., Sarbach, O., López-Cámara, D., 2021. Spherical accretion: Bondi, Michel, and rotating black holes. *MNRAS* 504, 5039–5053. doi:10.1093/mnras/stab1127, arXiv:2102.12529.
- Balsara, D.S., Garain, S., Florinski, V., Boscheri, W., 2020. An efficient class of WENO schemes with adaptive order for unstructured meshes. *Journal of Computational Physics* 404, 109062. doi:10.1016/j.jcp.2019.109062.
- Balsara, D.S., Garain, S., Tafflove, A., Montecinos, G., 2018. Computational electrodynamics in material media with constraint-preservation, multidimensional Riemann solvers and sub-cell resolution - Part II, higher order FVTD schemes. *Journal of Computational Physics* 354, 613–645. doi:10.1016/j.jcp.2017.10.013.
- Balsara, D.S., Kim, J., 2016. A subluminal relativistic magnetohydrodynamics scheme with ADER-WENO predictor and multidimensional Riemann solver-based corrector. *Journal of Computational Physics* 312, 357–384. doi:10.1016/j.jcp.2016.02.001, arXiv:1602.00633.
- Banyuls, F., Font, J.A., Ibáñez, J.M., Martí, J.M., Miralles, J.A., 1997. Numerical  $\{3 + 1\}$  General Relativistic Hydrodynamics: A Local Characteristic Approach. *ApJ* 476, 221–231. doi:10.1086/303604.
- Bondi, H., 1952. On spherically symmetrical accretion. *MNRAS* 112, 195. doi:10.1093/mnras/112.2.195.
- Boyer, R.H., Lindquist, R.W., 1967. Maximal Analytic Extension of the Kerr Metric. *Journal of Mathematical Physics* 8, 265–281. doi:10.1063/1.1705193.

- Chakrabarti, S.K., 1985. The natural angular momentum distribution in the study of thick disks around black holes. *ApJ* 288, 1–6. doi:10.1086/162755.
- Chakrabarti, S.K., 1989a. Standing Rankine-Hugoniot shocks in the hybrid model flows of the black hole accretion and winds. *ApJ* 347, 365–372. doi:10.1086/168125.
- Chakrabarti, S.K., 1989b. Studying Shocks in Model Astrophysical Flows. *ApJ* 337, L89. doi:10.1086/185385.
- Chakrabarti, S.K., 1990. Theory of Transonic Astrophysical Flows. World Scientific Publishing Co. doi:10.1142/1091.
- Chakrabarti, S.K., 1996a. Accretion processes on a black hole. *Phys. Rep.* 266, 229–390. doi:10.1016/0370-1573(95)00057-7, arXiv:astro-ph/9605015.
- Chakrabarti, S.K., 1996b. Global solutions of viscous transonic flows in Kerr geometry - I. Weak viscosity limit. *MNRAS* 283, 325. doi:10.1093/mnras/283.1.325, arXiv:astro-ph/9611019.
- Chakrabarti, S.K., 1996c. Solutions of Two-dimensional Viscous Accretion and Winds in Kerr Black Hole Geometry. *ApJ* 471, 237. doi:10.1086/177965, arXiv:astro-ph/9611020.
- Chakrabarti, S.K., Acharyya, K., Molteni, D., 2004. The effect of cooling on time dependent behaviour of accretion flows around black holes. *A&A* 421, 1–8. doi:10.1051/0004-6361:20034523, arXiv:astro-ph/0402557.
- Chakrabarti, S.K., Molteni, D., 1993. Smoothed Particle Hydrodynamics Confronts Theory: Formation of Standing Shocks in Accretion Disks and Winds around Black Holes. *ApJ* 417, 671. doi:10.1086/173345, arXiv:astro-ph/9310042.
- Cho, H., Prather, B.S., Narayan, R., Natarajan, P., Su, K.Y., Ricarte, A., Chatterjee, K., 2023. Bridging Scales in Black Hole Accretion and Feedback: Magnetized Bondi Accretion in 3D GRMHD. *ApJ* 959, L22. doi:10.3847/2041-8213/ad1048, arXiv:2310.19135.

- Cruz-Osorio, A., Lora-Clavijo, F.D., Guzmán, F.S., 2012. Is the flip-flop behaviour of accretion shock cones on to black holes an effect of coordinates? *MNRAS* 426, 732–738. doi:10.1111/j.1365-2966.2012.21794.x, arXiv:1210.6588.
- Das, S., Chattopadhyay, I., Nandi, A., Molteni, D., 2014. Periodic mass loss from viscous accretion flows around black holes. *MNRAS* 442, 251–258. doi:10.1093/mnras/stu864, arXiv:1405.4415.
- Debnath, S., Chattopadhyay, I., Joshi, R.K., 2024. Oscillating shocks in the transonic viscous, variable  $\Gamma$  accretion flows around black holes. *MNRAS* 528, 3964–3980. doi:10.1093/mnras/stae181, arXiv:2401.07786.
- Del Zanna, L., Bucciantini, N., 2002. An efficient shock-capturing central-type scheme for multidimensional relativistic flows. I. Hydrodynamics. *A&A* 390, 1177–1186. doi:10.1051/0004-6361:20020776, arXiv:astro-ph/0205290.
- Dihingia, I.K., Mizuno, Y., 2024. Dynamical Properties of Magnetized Low-angular-momentum Accretion Flows around a Kerr Black Hole. *ApJ* 967, 4. doi:10.3847/1538-4357/ad391a, arXiv:2403.18359.
- Fambri, F., Dumbser, M., Köppel, S., Rezzolla, L., Zanotti, O., 2018. ADER discontinuous Galerkin schemes for general-relativistic ideal magnetohydrodynamics. *MNRAS* 477, 4543–4564. doi:10.1093/mnras/sty734, arXiv:1801.02839.
- Font, J.A., 2008. Numerical Hydrodynamics and Magnetohydrodynamics in General Relativity. *Living Reviews in Relativity* 11, 7. doi:10.12942/lrr-2008-7.
- Font, J.A., Daigne, F., 2002. The runaway instability of thick discs around black holes - I. The constant angular momentum case. *MNRAS* 334, 383–400. doi:10.1046/j.1365-8711.2002.05515.x, arXiv:astro-ph/0203403.
- Fukue, J., 1987. Transonic disk accretion revisited. *PASJ* 39, 309–327.
- Gammie, C.F., McKinney, J.C., Tóth, G., 2003. HARM: A Numerical Scheme for General Relativistic Magnetohydrodynamics. *ApJ* 589, 444–457. doi:10.1086/374594, arXiv:astro-ph/0301509.

- Garain, S.K., Ghosh, H., Chakrabarti, S.K., 2014. Quasi-periodic oscillations in a radiative transonic flow: results of a coupled Monte Carlo-TVD simulation. *MNRAS* 437, 1329–1336. doi:10.1093/mnras/stt1969, arXiv:1310.6493.
- Garain, S.K., Kim, J., 2023. Three-dimensional simulations of advective, sub-Keplerian accretion flow on to non-rotating black holes. *MNRAS* 519, 4550–4563. doi:10.1093/mnras/stac3736, arXiv:2212.08310.
- Giri, K., Chakrabarti, S.K., Samanta, M.M., Ryu, D., 2010. Hydrodynamic simulations of oscillating shock waves in a sub-Keplerian accretion flow around black holes. *MNRAS* 403, 516–524. doi:10.1111/j.1365-2966.2009.16147.x, arXiv:0912.1174.
- Hawley, J.F., Smarr, L.L., Wilson, J.R., 1984. A numerical study of non-spherical black hole accretion. I Equations and test problems. *ApJ* 277, 296–311. doi:10.1086/161696.
- Janiuk, A., Proga, D., Kurosawa, R., 2008. Nonaxisymmetric Effects in Black Hole Accretion Inviscid Hydrodynamics: Formation and Evolution of a Tilted Torus. *ApJ* 681, 58–72. doi:10.1086/588375, arXiv:0803.2087.
- Kaaz, N., Murguia-Berthier, A., Chatterjee, K., Liska, M.T.P., Tchekhovskoy, A., 2023. Jet Formation in 3D GRMHD Simulations of Bondi-Hoyle-Lyttleton Accretion. *ApJ* 950, 31. doi:10.3847/1538-4357/acc7a1, arXiv:2201.11753.
- Kim, J., Garain, S.K., Balsara, D.S., Chakrabarti, S.K., 2017a. General relativistic numerical simulation of sub-Keplerian transonic accretion flows on to black holes: Schwarzschild space-time. *MNRAS* 472, 542–549. doi:10.1093/mnras/stx1986, arXiv:1707.09856.
- Kim, J., Garain, S.K., Balsara, D.S., Chakrabarti, S.K., 2017b. General relativistic numerical simulation of sub-Keplerian transonic accretion flows on to black holes: Schwarzschild space-time. *MNRAS* 472, 542–549. doi:10.1093/mnras/stx1986, arXiv:1707.09856.
- Kim, J., Garain, S.K., Chakrabarti, S.K., Balsara, D.S., 2019. General relativistic numerical simulation of sub-Keplerian transonic accretion flows on to rotating black holes: Kerr space-time. *MNRAS* 482, 3636–3645. doi:10.1093/mnras/sty2953, arXiv:1810.12469.

- Lalagos, A., Gottlieb, O., Kaaz, N., Chatterjee, K., Liska, M., Christie, I.M., Tchekhovskoy, A., Zhuravleva, I., Nokhrina, E., 2022. Bridging the Bondi and Event Horizon Scales: 3D GRMHD Simulations Reveal X-shaped Radio Galaxy Morphology. *ApJ* 936, L5. doi:10.3847/2041-8213/ac7bed, arXiv:2202.08281.
- Lee, S.J., Chattopadhyay, I., Kumar, R., Hyung, S., Ryu, D., 2016. Simulations of Viscous Accretion Flow around Black Holes in a Two-dimensional Cylindrical Geometry. *ApJ* 831, 33. doi:10.3847/0004-637X/831/1/33, arXiv:1608.03997.
- Lee, S.J., Ryu, D., Chattopadhyay, I., 2011. Quasi-spherical, Time-dependent Viscous Accretion Flow: One-dimensional Results. *ApJ* 728, 142. doi:10.1088/0004-637X/728/2/142, arXiv:1012.4548.
- LeVeque, R., 2002. Finite Volume Methods for Hyperbolic Problems. Cambridge Texts in Applied Mathematics, Cambridge University Press. URL: <https://books.google.co.in/books?id=QazcnD7GUoUC>.
- Li, J., Ostriker, J., Sunyaev, R., 2013. Rotating Accretion Flows: From Infinity to the Black Hole. *ApJ* 767, 105. doi:10.1088/0004-637X/767/2/105, arXiv:1206.4059.
- Mignone, A., 2014. High-order conservative reconstruction schemes for finite volume methods in cylindrical and spherical coordinates. *Journal of Computational Physics* 270, 784–814. doi:10.1016/j.jcp.2014.04.001, arXiv:1404.0537.
- Mignone, A., Bodo, G., 2005. An HLLC Riemann solver for relativistic flows - I. Hydrodynamics. *MNRAS* 364, 126–136. doi:10.1111/j.1365-2966.2005.09546.x, arXiv:astro-ph/0506414.
- Misner, C.W., Thorne, K.S., Wheeler, J.A., 1973. *Gravitation*.
- Molteni, D., Lanzafame, G., Chakrabarti, S.K., 1994. Simulation of thick accretion disks with standing shocks by smoothed particle hydrodynamics. *ApJ* 425, 161–170. doi:10.1086/173972, arXiv:astro-ph/9310047.
- Narayan, R., Yi, I., 1994. Advection-dominated Accretion: A Self-similar Solution. *ApJ* 428, L13. doi:10.1086/187381, arXiv:astro-ph/9403052.

- Novikov, I.D., Thorne, K.S., 1973. Astrophysics of black holes., in: Dewitt, C., Dewitt, B.S. (Eds.), *Black Holes (Les Astres Occlus)*, pp. 343–450.
- Olivares, H.R., Mościbrodzka, M.A., Porth, O., 2023. General relativistic hydrodynamic simulations of perturbed transonic accretion. *A&A* 678, A141. doi:10.1051/0004-6361/202346010, arXiv:2301.12020.
- Paczynski, B., Wiita, P.J., 1980. Thick accretion disks and supercritical luminosities. *A&A* 88, 23–31.
- Patra, D., Chatterjee, A., Dutta, B.G., Chakrabarti, S.K., Nandi, P., 2019. Evidence of Outflow-induced Soft Lags of Galactic Black Holes. *ApJ* 886, 137. doi:10.3847/1538-4357/ab4c34, arXiv:1901.02245.
- Porth, O., Chatterjee, K., Narayan, R., Gammie, C.F., Mizuno, Y., Aninos, P., Baker, J.G., Bugli, M., Chan, C.k., Davelaar, J., et al., 2019. The Event Horizon General Relativistic Magnetohydrodynamic Code Comparison Project. *ApJS* 243, 26. doi:10.3847/1538-4365/ab29fd, arXiv:1904.04923.
- Porth, O., Olivares, H., Mizuno, Y., Younsi, Z., Rezzolla, L., Moscibrodzka, M., Falcke, H., Kramer, M., 2017. The black hole accretion code. *Computational Astrophysics and Cosmology* 4, 1. doi:10.1186/s40668-017-0020-2, arXiv:1611.09720.
- Proga, D., Begelman, M.C., 2003. Accretion of Low Angular Momentum Material onto Black Holes: Two-dimensional Magnetohydrodynamic Case. *ApJ* 592, 767–781. doi:10.1086/375773, arXiv:astro-ph/0303093.
- Ressler, S.M., Quataert, E., White, C.J., Blaes, O., 2021. Magnetically modified spherical accretion in GRMHD: reconnection-driven convection and jet propagation. *MNRAS* 504, 6076–6095. doi:10.1093/mnras/stab311, arXiv:2102.01694.
- Ryu, D., Chakrabarti, S.K., Molteni, D., 1997. Zero-Energy Rotating Accretion Flows near a Black Hole. *ApJ* 474, 378–388. doi:10.1086/303461, arXiv:astro-ph/9607051.
- Shapiro, S.L., Teukolsky, S.A., 1983. Black holes, white dwarfs and neutron stars. *The physics of compact objects*. doi:10.1002/9783527617661.

- Suková, P., Charzyński, S., Janiuk, A., 2017. Shocks in the relativistic transonic accretion with low angular momentum. *MNRAS* 472, 4327–4342. doi:10.1093/mnras/stx2254, arXiv:1709.01824.
- Toro, E., 2009. Riemann Solvers and Numerical Methods for Fluid Dynamics: A Practical Introduction. Springer Berlin Heidelberg. URL: <https://books.google.co.in/books?id=SqEjX0um8o0C>.
- Wilson, J.R., 1972. Numerical Study of Fluid Flow in a Kerr Space. *ApJ* 173, 431. doi:10.1086/151434.